


Localized dissipative vortices in chiral nematic liquid crystal cells

M. G. Clerc, G. González-Cortés , and S. Echeverría-Alar 

Departamento de Física and Millenium Institute for Research in Optics, Facultad de Ciencias Físicas y Matemáticas, Universidad de Chile, Casilla 487-3, Santiago, Chile

 (Received 22 October 2021; accepted 8 April 2022; published 26 April 2022)

Solitary waves and solitons have played a fundamental role in understanding nonlinear phenomena and emergent particle-type behaviors in out-of-equilibrium systems. This type of dynamic phenomenon has not only been essential to comprehend the behavior of fundamental particles but also to establish the possibilities of novel technologies based on optical elements. Dissipative vortices are topological particle-type solutions in vectorial field out-of-equilibrium systems. These states can be extended or localized in space. The topological properties of these states determine the existence, stability properties, and dynamic evolution. Under homeotropic anchoring, chiral nematic liquid crystal cells are a natural habitat for localized vortices or spherulites. However, chiral bubble creation and destruction mechanisms and their respective bifurcation diagrams are unknown. We propose a minimal two-dimensional model based on experimental observations of a temperature-triggered first-order winding/unwinding transition of a cholesteric liquid crystal cell and symmetry arguments, and investigate this system experimentally. This model reveals the main ingredients for the emergence of chiral bubbles and their instabilities. Experimental observations have a quite fair agreement with the theoretical results. Our findings are a starting point to understand the existence, stability, and dynamical behaviors of dissipative particles with topological properties.

DOI: [10.1103/PhysRevResearch.4.L022021](https://doi.org/10.1103/PhysRevResearch.4.L022021)

Dissipative particle-type solutions have been studied in many fields of nonlinear science, ranging from biology, chemistry, to physics (see the reviews [1–4] and references therein). Localized structures are characterized by being supported by a spatially extended stable state. These localized states present features of the particles. Hence, one can characterize them with a family of discrete parameters such as position, amplitude, width, and topological charge. The localized structures generalize the concept of solitons or solitary waves reported in fluid dynamics, nonlinear optics, and Hamiltonian systems [5]. Because of the initial conditions or inherent fluctuations, out-of-equilibrium physical systems exhibit rich dynamics of the localized structures [1–4]. Particle-type solutions with topological charges are well known as *vortices* [6]. In complex fields, vortices are point-like singularities that locally break the rotational symmetry. Namely, zero intensity at the singular point characterizes the vortex with a phase spiraling around it. The number of phase jumps determines the topological charge of the vortex [6]. The spiral rotation sense gives the sign of the charge. Vortices are nucleated and annihilated by pairs between opposite charges due to the conservation of the total topological charge. The Ginzburg-Landau equation is a universal and minimal model that presents vortices [6,7]. This universal model has

been used to describe superconductors, magnetic media, fluids, superfluids, granular matter, liquid crystals, and optical dielectrics, to mention a few [6–10].

Liquid crystals are a natural physical context where extended or localized dissipative vortices can be observed [11]. Extended vortices in nematic liquid crystals are usually called umbilical defects. Topological localized states are the cholesteric bubbles observed in chiral liquid crystals, *spherulites* or *elementary torons* [12–15]. These localized states are characterized by exhibiting localized vorticity with a circular shape surrounded by a homogeneous state without vorticity, when observed under crossed polarizers (see Fig. 1). These cholesteric localized objects and textures also possess a rich three-dimensional structure [15]. The spherulites are usually observed close to the winding/unwinding transition [12–14], which occurs when the helical structure of a chiral nematic liquid crystal develops/frustrates under homeotropic anchoring [16,17]. Topological transitions, nontopological to topological states and vice versa, have previously been observed in liquid crystals [12,18–21]. Although cholesteric bubbles and their transitions have been studied for several decades, their theoretical description, interaction, creation mechanisms, and instabilities have not been completely clarified.

This Letter aims to investigate the emergence, stabilization, and instabilities of chiral bubbles in the context of cholesteric liquid crystal cells subjected to thermal driving. Experimentally, the winding/unwinding transition, triggered by temperature, of a chiral nematic liquid crystal sample is analyzed. We show that this transition is of the first-order type. Different cholesteric textures are observed when changing

Published by the American Physical Society under the terms of the [Creative Commons Attribution 4.0 International license](https://creativecommons.org/licenses/by/4.0/). Further distribution of this work must maintain attribution to the author(s) and the published article's title, journal citation, and DOI.

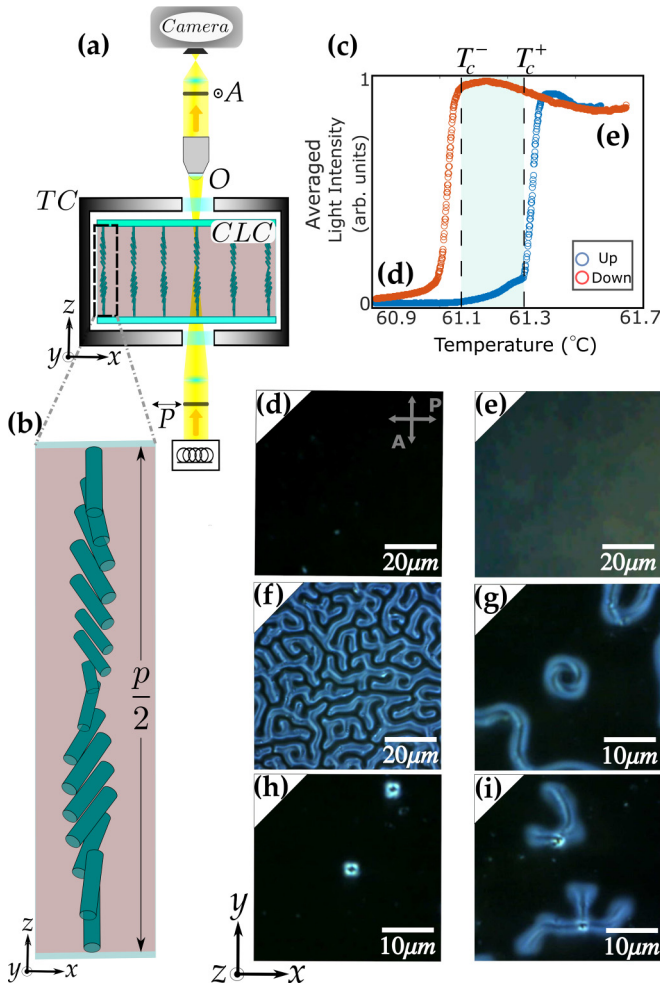


FIG. 1. Cholesteric liquid crystal cell under homeotropic anchoring and crossed polarizers. (a) Schematic representation of the experimental setup. TC represents the thermal chamber. O stands for the objective of the microscope, with magnifications ranging from $20\times$ to $50\times$. P and A are the polarizer and analyzer, respectively. (b) Director representation \vec{n} of the chiral nematic liquid crystal displaying a TIC phase. p is the cholesteric pitch. (c) The subcritical bifurcation between the (d) unwound state and the (e) TIC phase. The light blue shaded region stands for the bistability region. (f) Cholesteric labyrinth. (g) Loop of CF-1. (h) Chiral bubbles. (i) Fingering instability of the localized vortices.

the temperature, such as translational invariant configuration (TIC), modulated TIC, cholesteric fingers of type 1 (CF-1), loops of CF-1, and spherulites. Similar textures have been reported in experiments controlled by applying a voltage to cholesteric liquid crystal cells [12]. Based on the subcritical nature of the observed transition and symmetry arguments, an amplitude equation of the Ginzburg-Landau type is proposed. This minimal two-dimensional model allows us to disclose the phase diagram and the transitions in the system. We establish, theoretically and numerically, the stability region of the chiral bubbles. The combined effect of chirality, interface curvature, and topology allows us to reveal a saddle-node mechanism of the appearance or disappearance of the chiral bubbles. The finger instability of the cholesteric bubbles is characterized by

a modal stability analysis. There is a fair agreement between the experimental observations and the theoretical findings.

Experimental setup. Polarized optical microscopy with a hot stage is a well-known experiment setup that permits the characterization of liquid crystal textures and their transitions (see Ref. [22] and references therein). Figure 1(a) shows a schematic representation of this experiment. This setup is made up of a white light source, which passes through a polarizer P and illuminates a cholesteric liquid crystal (CLC) sample. To control the temperature, the sample is inside a thermal chamber (TC). The transmitted light goes into the objective O and after that passes through another polarizer A . A CMOS camera monitors transmitted light. We consider CLC samples with homeotropic anchoring. The imposition of this boundary condition frustrates the helical structure of the CLC [cf. Fig. 1(b)]. The degree of frustration of this mesophase is quantified by the confinement parameter d/p , where d is the cell thickness and p is the cholesteric pitch [17]. This pitch accounts for the length of rotation of the molecules, and it depends on temperature, and the concentration of chiral molecules [12,22]. The liquid crystal used is a mixture of nematic E7 (Merck) with a chiral molecule EOS-12 [23]. The molecule concentration determines the cholesteric pitch p [11]. The pitch length is determined by the Grandjean-Cano technique [12].

Experimental results. To carry out the study of the winding/unwinding transition of CLC samples, we consider two cells with different concentrations of chiral elements since a higher chiral molecule concentration yields a higher mixture chirality and shorter pitch. The first sample has a dopant concentration of 3 wt % ($p = 21.8 \mu\text{m}$ at $T = 57^\circ\text{C}$) and its thickness is $d = 9 \mu\text{m}$. When varying the temperature, the sample shows a subcritical winding/unwinding transition at $T_c^+ \approx 61.3^\circ\text{C}$, as depicted in Fig. 1(c). The transmitted light intensity is used to measure the subcritical winding/unwinding transition. The blue (red) curve stands for the increase (decrease) of temperature at a rate of $0.5^\circ\text{C}/\text{min}$. At $T < T_c^- \approx 61.1^\circ\text{C}$ the helical structure of this CLC unwinds completely, and under crossed polarizers a homeotropic texture is observed [see Fig. 1(d)], which is characterized by no transmitted light. When the sample overcomes the critical temperature T_c^+ , the uniform helical structure is recovered and a homogeneous coloration is observed on the transmitted light, TIC phase [cf. Fig. 1(e)]. The hysteresis loop between the homeotropic and TIC phase renders the transition of the first-order type. Indeed, the system exhibits a bistability region [see the light blue shaded region in Fig. 1(c)].

The second sample of the CLC mixture contains 25 wt % ($p = 2.6 \mu\text{m}$ at $T = 57^\circ\text{C}$) of the chiral molecule and thickness $d = 200 \mu\text{m}$. We observe a subcritical bifurcation, however, the scenario changes radically. In this case, at $T > T_c^+ \approx 51.3^\circ\text{C}$ the nucleation of the cholesteric fingers is observed. Rapidly, the rounded tip of the fingers suffers a tip-splitting instability, and the abnormal tip advance and merge with the nearest cholesteric finger, showing similar dynamical behaviors to those reported in Ref. [24]. This process ends in a cholesteric labyrinthine pattern. Figure 1(f) shows a typical observed labyrinthine pattern. The self-merging of the fingers gives rise to CF-1 loops, analogous to those observed with the application of an oscillatory voltage [25]. Upon decreasing

the temperature, the CF-1 retracts and the loops survive [see Fig. 1(g)]. Lowering further, the CF-1 loop collapses into cholesteric bubbles [cf. Fig. 1(h)]. Here, we use the term cholesteric bubble for the localized objects created by this process, which correspond to the *elementary torons* [15]. The transition from CF-1 loops to spherulites is irreversible [14]. When increasing the temperature, the cholesteric fingers appear at the interface of the localized vortices, as shown in Fig. 1(i). This fingering instability has been also observed in electrically driven experiments [26].

Theoretical description. Close to the winding/unwinding transition and in the long-pitch limit $p \gg l$, where l is a typical molecular length, the average molecular orientation of the frustrated chiral nematic liquid crystal state inside a cell of thickness d can be modeled as [27,28]

$$\bar{n} = \begin{pmatrix} \cos\left(\frac{z}{p} + \theta\right) \sin\left[\alpha \sin\left(\frac{\pi z}{d}\right)\right] \\ \sin\left(\frac{z}{p} + \theta\right) \sin\left[\alpha \sin\left(\frac{\pi z}{d}\right)\right] \\ \cos\left[\alpha \sin\left(\frac{\pi z}{d}\right)\right] \end{pmatrix}, \quad (1)$$

where \bar{n} is the liquid crystal director, which accounts for the orientational average of molecules in a small volume element, $\alpha = \alpha(x, y, t)$ is the tilt angle of \bar{n} from the vertical z axis, and $\theta = \theta(x, y, t)$ is the azimuth angle of the director, that is, the angle between the projection of \bar{n} into the x - y plane and the x axis. To characterize the winding/unwinding transition, one can introduce the order parameter $Q \equiv n_z(n_x + in_y)$ [27]. Close to the transition, $\alpha \ll 1$, the order parameter becomes $Q(x, y, z, t) \approx \alpha e^{i(\theta + \pi z/p)} \sin(\pi z/d) = A e^{i\pi z/p} \sin(\pi z/d)$. The two-dimensional complex amplitude $A(x, y, t) = \alpha e^{i\theta}$ can be used as an order parameter to study the winding/unwinding transition at the middle plane of the cell [27]. This simplification assumes that 3D effects, such as confinement and surface anchoring, are neglectable.

To shed light on the cholesteric textures that emerge in the thermally driven winding/unwinding transition, we propose a phenomenological amplitude equation for A . Based on the subcritical nature of the transition [see Fig. 1(c)], symmetry arguments, and multiscaling, the dimensionless amplitude equation reads

$$\begin{aligned} \partial_t A &= \mu A + \beta |A|^2 A - |A|^4 A + \partial_{\bar{\eta}} \partial_{\bar{\eta}} A \\ &+ \delta \partial_{\bar{\eta}} \partial_{\bar{\eta}} \bar{A} + \chi (A \partial_{\bar{\eta}} A - \bar{A} \partial_{\bar{\eta}} A), \end{aligned} \quad (2)$$

where $\partial_{\bar{\eta}} = \partial_x + i\partial_y$ is a differential operator on the complex plane, the *Wirtinger derivative*. The bifurcation parameter $\mu \propto T - T_c^+$ measures the distance from the critical temperature. Indeed, μ is a function of temperature, concentration, cholesteric pitch, thickness of the cell, and elastic constants. The three first terms on the right-hand side of Eq. (2) model a subcritical transition ($\beta > 0$). The fourth and fifth terms account for the isotropic and anisotropic elastic coupling in the system, respectively [29]. The last term models the mirror symmetry breaking, i.e., chirality [27]. The model Eq. (2) obeys the scaling $\partial_t \sim \mu$, $\partial_{\bar{\eta}} \sim \mu^{1/2}$, $A \sim \mu^{1/4}$, $\chi \sim \mu^{1/4}$, with $\mu \ll 1$ and $\delta \sim \mathcal{O}(1)$. The dynamics of Eq. (2) is vari-

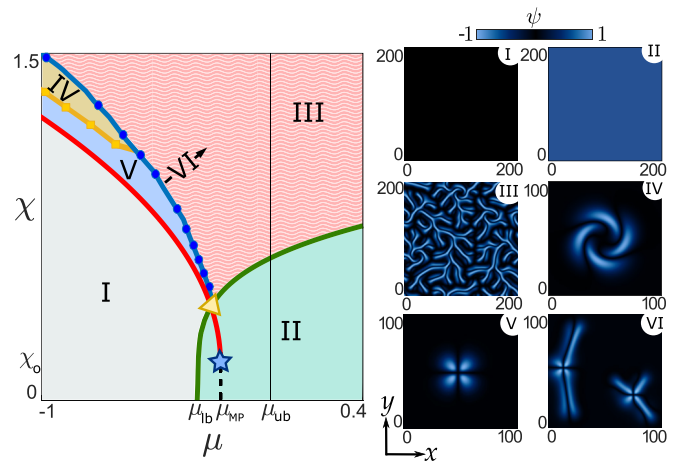


FIG. 2. Phase diagram of model Eq. (2) with $\beta = 1$ and $\delta = 0.05$. $\mu_{lb} = -1/4$ and $\mu_{ub} = 0$ are the limits of the bistability region between A_o and A_T . $\mu_{MP} = -3/16$ is the Maxwell point. The green line accounts for the spatial instability of A_T . The red curve is the saddle-node bifurcation of the localized vortices. The yellow line with \square markers stands for the transition between loops and spherulites. The blue line with \circ markers shows the mode-3 instability of chiral bubbles. $\chi_o = 0.26$ is the minimum value for the existence of spherulites (\star). The Δ symbol is the triple point of the system. Regions I, II, III, IV, and V account for the stable zone of uniform state A_o , TIC phase A_T , cholesteric patterns, cholesteric loop, and chiral bubble, respectively. Path VI represents the fingering instability. $\psi = \text{Re}(A)\text{Im}(A)$ is the polarization field. The right panels illustrate the states in the respective regions.

ational, $\partial_t A = -\delta \mathcal{F}[A, \bar{A}]/\delta \bar{A}$, where

$$\begin{aligned} \mathcal{F} &= \iint dx dy \left\{ -\mu |A|^2 - \beta \frac{|A|^4}{2} + \frac{|A|^6}{3} + |\nabla A|^2 \right. \\ &\left. + 2\delta \text{Re}\{(\partial_{\bar{\eta}} \bar{A})^2\} - \chi |A|^2 (\partial_{\bar{\eta}} A + \partial_{\bar{\eta}} \bar{A}) \right\} \end{aligned} \quad (3)$$

is a Lyapunov functional. Hence, the dynamics of the amplitude Eq. (2) is driven by the minimization of \mathcal{F} . A similar amplitude equation to model (2), but supercritical and with terms of different order in the scaling has been used to study the unwinding transition [27].

For $\mu < \mu_{ub} \equiv 0$, the unwound state $A = A_o \equiv 0$ of Eq. (2) is stable (see region I in Fig. 2). When $\mu \geq \mu_{ub}$ the zero state is unstable by a subcritical instability and the TIC state $A_T = (1/2 + \sqrt{1/4 + \mu})^{1/2} e^{i\theta_o}$ is stable (see region II in Fig. 2), with θ_o an arbitrary phase. Indeed, the model Eq. (2) presents a bistability region between $A = 0$ and A_T in $\mu_{lb} \leq \mu \leq \mu_{ub}$ for small chirality. Within this zone there is a Maxwell point μ_{MP} , where $\mathcal{F}[A_T] = \mathcal{F}[A_o]$ [30]. The A_T solution has a spatial instability that gives rise to striped pattern, which is associated with the modulated TIC phase [12]. A linear stability analysis around A_T delivers the critical wave vector $|\vec{k}_c| = \sqrt{[f(\mu) + \delta g(\mu) + 2\chi^2 A_T^2]/(1 - \delta^2)}$, where $f(\mu) = \mu + 2\beta A_T^2 - 3A_T^4$ and $g(\mu) = \beta A_T^2 - 2A_T^4$. The spatial instability curve is obtained by restricting $|\vec{k}_c|$ to be a real quantity (cf. green line in Fig. 2). The critical wavelength is $\lambda_c = 2\pi/|\vec{k}_c|$, which is proportional to the pitch p [12]. For

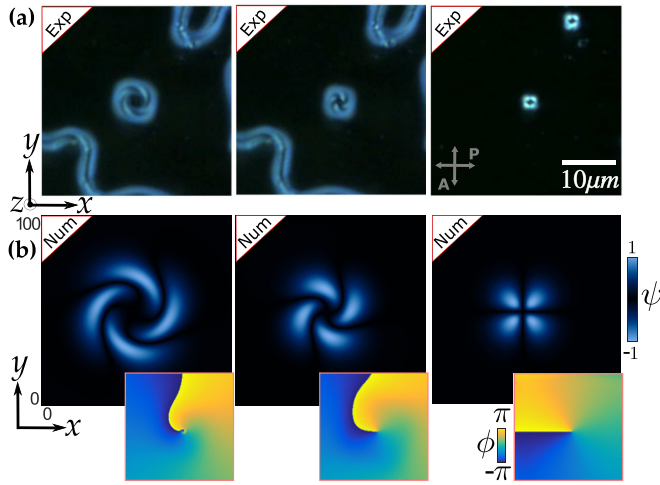


FIG. 3. Transition from CF-1 loops to chiral bubbles. (a) Experimental bifurcation triggered by decrease in temperature in the sample with 25 wt % of chiral dopant. (b) Numerical transition in model Eq. (2) with $\beta = 1$, and $\delta = 0.05$, when parameters change from region IV to V in the phase diagram of Fig. 2. $\psi = \text{Re}(A)\text{Im}(A)$ is the polarization field. ϕ is the phase field. The middle panels are transient states.

high chirality ($\chi > 1.5$), the parameter χ is approximated by $\chi \approx (2\pi/\sqrt{2A_T})/p$. Hence, χ is interpreted as a qualitative measure of the confinement, and have a temperature dependence through p . Experimentally, a similar bifurcation diagram has been obtained by varying the applied voltage and the confinement parameter (chirality) [26].

Chiral bubble solutions and instabilities. The model Eq. (2) exhibits localized finger states with different tips. When changing parameters, the pointed tips can merge, and the rounded tips exhibit the tip-splitting instability, which is characterized by a flowerlike type of growth [12]. The final equilibrium structure is a labyrinthine pattern with embedded loops (see panel III of Fig. 2 and Video 1 in the Supplemental Material [31]). Entering in the zone IV, the fingers withdraw and only loops survive. Starting from region IV and going into region V, the loop collapses into an axisymmetric localized vortex solution $A(r, \theta) = R(r)e^{i\phi(\theta)}$, where R and ϕ are the modulus and phase, and $\{r, \theta\}$ are the polar coordinates. Figure 3 shows this transition experimentally and numerically. Besides the change in size, the phase field transforms from a nontrivial phase structure into the typical phase jump of a singular point or vortex (spherulites) [19]. This transition has been studied experimentally and numerically from a three-dimensional configuration [32].

In the experiment, when decreasing temperature, the spherulites shrink as depicted in Fig. 4(a). Suddenly, the localized vortex is lost. This out-of-the-blue disappearance is characteristic of a saddle-node bifurcation and is referred to as *ruin* [33]. An analogous transition is observed numerically between regions V and I of Fig. 2. This transition should be accompanied by the divergence of the spherulite residence time τ_r , which is the elapsed time by the vortex before its disappearance, near the saddle-node bifurcation. To shed light on this mechanism, we measure from model Eq. (2) the accumulated area $A_{ac}(\chi) = \int_{t_0}^{\tau_r} \int_0^\infty R(r, t)^2 dr dt$, which is

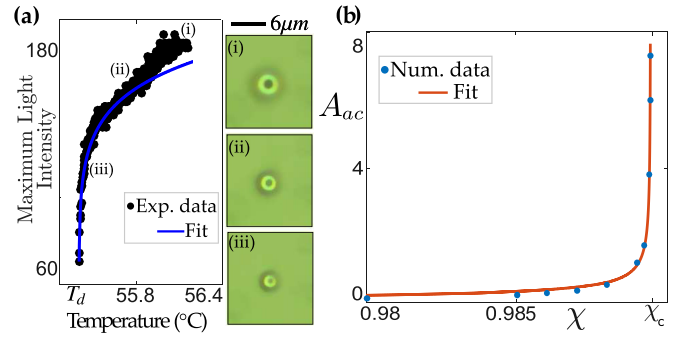


FIG. 4. Disappearance of chiral bubbles. (a) Experimental observation of the spherulite loss in the sample with 25 wt % of chiral dopant. The black dots correspond to the maximum intensity peak of the localized structure when the temperature is decreased from 56.3°C (i) until the disappearance at $T_d \approx 55.3^\circ\text{C}$. The blue curve is the fit $128(T - T_d)^{0.08}$. The insets show the spherulite changes under circular polarization. (b) Divergence of A_{ac} at $\chi_c = 0.989$, in Eq. (2) with $\mu = -0.45$, $\beta = 1$, $\delta = 0.05$, and $t_0 = 0$. The fit is $A_{ac} = 0.024(\chi_c - \chi)^{-1/2}$, where $\chi_c = 0.9895$.

proportional to τ_r near the bifurcation [34]. The lower limit t_0 is an arbitrary reference time. Figure 4(b) summarizes the result. When varying χ , a power law $A_{ac} \propto (\chi_c - \chi)^{-1/2}$ is obtained, rendering the transition of the saddle-node type [33].

In region V of Fig. 2, cholesteric bubbles of different sizes are stable. The main feature of the transition between bubbles is the interface dynamics, with a core r_f , which connects $R = 0$ and $R \approx |A_T|$ [see Fig. 5(a)]. For large bubbles size, the radial profile of the interface is approximated by $R_o = [3/4(1 + e^{\sqrt{3/4}(r-r_f)})]^{1/2}$ at the Maxwell point [35]. Introducing the ansatz $A(r, \theta, t) = R_o[r - r_f(t)]e^{i\theta} + w$, where w is a small correction function, into Eq. (2) with $\beta = 1$ and $\delta \ll 1$, linearizing in w and applying a solvability condition after straightforward calculation, we get

$$r_f = c_1 \Delta\mu + \frac{c_2 \chi - c_o}{r_f} - \frac{c_1}{r_f^2}, \quad (4)$$

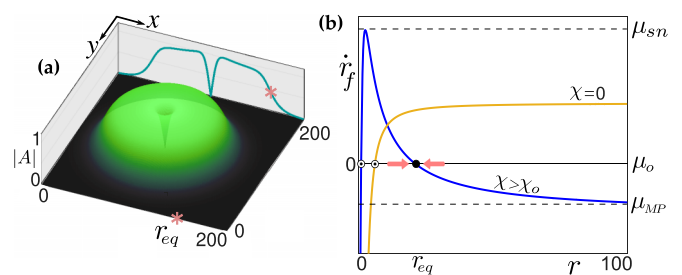


FIG. 5. (a) Chiral bubble observed in model Eq. (2) with $\mu_o = -0.21$, $\chi = 0.4$, $\delta = 0.05$, and $\beta = 1$. The radial profile $|A| = R(r)$ is characterized by the core r_f of the interface. (b) Phase portrait of Eq. (4). The yellow curve accounts for the case $\chi = 0$. The blue curve shows the force r_f when $\chi > \chi_o$. The open dots represent unstable solutions. The solid black dot is a stable equilibrium (r_{eq}). μ_{sn} is the saddle-node critical parameter. μ_{MP} is the Maxwell point.

where $c_o = \int_{-\infty}^{\infty} (\partial_z R_o)^2 dz$, $c_1 = -\int_{-\infty}^{\infty} \partial_z R_o R_o dz$, $c_2 = -2 \int_{-\infty}^{\infty} \partial_z R_o R_o^2 dz$, $z = r - r_f$, $\Delta\mu = \mu - \mu_{MP}$, and $r_f = c_o \partial_t r_f$.

The kinematic Eq. (4) combines energy difference, chirality, curvature, and topology effects, respectively. Figure 5(b) illustrates the kinematic Eq. (4). There are two cases: zero chirality $\chi = 0$ (yellow curve) in which the system only has one unstable state, and $\chi > \chi_o = c_o/c_2$ (blue curve), where the systems exhibit two localized topological states, one unstable and another stable ($r_f = r_{eq}$). Hence, chiral bubbles are a consequence of the presence of the chirality. Likewise, we note that the previous method is only applicable for positive topological charges since the negative one requires considering the transversal dynamics of the interface. The disappearance of the chiral bubble ($\mu = \mu_{sn}$) is mediated by the collision of two equilibria, which indicates a saddle-node bifurcation. The critical curve of this bifurcation is $\chi = \chi_o + 2c_1|\Delta\mu|^{1/2}$ (red line in Fig. 2). Note that at $\mu = \mu_{MP}$ and $\chi = \chi_o$, the chiral bubble is unstable due to the divergence of its size.

In model Eq. (2), the chiral bubble suffers a fingering instability (cf. path VI in the phase diagram of Fig. 2). A numerical linear analysis can be performed to investigate this transition. Introducing the ansatz $A = [R_o + \tilde{R}(r) \cos(m\theta) e^{\lambda_m t}] e^{i[\theta + \tilde{\phi}(r) \sin(m\theta) e^{\lambda_m t}]}$ in Eq. (2), where $\tilde{R}(r)$ and $\tilde{\phi}(r)$ are small perturbations, the modes $m = 1, 2$, and 3 are unstable, where $\lambda_3 > \lambda_2 > \lambda_1 > 0$. Modes with $m > 3$ cannot be treated with the perturbational ansatz given above, due to the appearance of new phase jumps in the complex field. Experimentally, we have not observed these higher modes. The blue line shown in Fig. 2 is the mode-3 instability. This curve allows us to envisage a triple point between a patterned state and two uniform phases (see the triangle in Fig. 2) [36].

In conclusion, the minimal model Eq. (2) allows us to reveal analytically the instabilities of chiral bubbles, namely, saddle-node bifurcation and interfacial instability. Both behaviors are mainly controlled by the chirality χ of the system, which is the manifestation of the inherent twist of the chiral liquid crystal in the middle plane of the cell. Also, the model reproduces other types of cholesteric textures, such as the TIC phase, cholesteric labyrinth, and CF-1 loop. The instabilities and textures have been experimentally observed using polarized optical microscopy. Indeed, there is agreement between the experimental observations and the 2D minimal model Eq. (2). Three-dimensional effects were neglected in this work and could be necessary to describe in more depth the transition from CF-1 loop to the cholesteric bubble. However, the detailed analysis of this transition was out of the scope of this study. Comparisons between the theoretical 2D model and the 3D results in Ref. [32] are in progress. In addition, with our modeling approach, it is possible to visualize and understand other behaviors of cholesteric liquid crystals. For example, nematic umbilical defects undergo structural transitions due to chirality [37], the chiral bubble interaction, and topological labyrinthine pattern propagation. Work is in progress in these directions.

We acknowledge P. I. Hidalgo and J. Vegara for the synthesis of the cholesteric liquid crystal. The authors thank for the financial support of ANID-Millennium Science Initiative Program-ICN17_012 (MIRO) and FONDECYT Project No. 1210353. G.G.-C. acknowledges the financial support from ANID-PFCHA Doctorado Nacional Grant No. 2017-21171672. S.E.-A. acknowledges the financial support from ANID by Beca Doctorado Nacional 2020-21201376.

-
- [1] N. Akhmediev and A. Ankiewicz, *Dissipative Solitons: From Optics to Biology and Medicine* (Springer, Heidelberg, 2008), Vol. 751.
- [2] H.-G. Purwins, H. U. Bödeker, and S. Amiranashvili, Dissipative solitons, *Adv. Phys.* **59**, 485 (2010).
- [3] O. Descalzi, M. Clerc, S. Residori, and G. Assanto, *Localized States in Physics: Solitons and Patterns* (Springer, Berlin, 2011).
- [4] M. Tlidi, K. Staliunas, K. Panajotov, A. G. Vladimirov, and M. G. Clerc, Localized structures in dissipative media: from optics to plant ecology, *Phil. Trans. R. Soc. A* **372**, 20140101 (2014).
- [5] A. C. Newell, *Solitons in Mathematics and Physics* (Society for Industrial and Applied Mathematics, Philadelphia, 1985).
- [6] L. M. Pismen, *Vortices in Nonlinear Fields: From Liquid Crystals to Superfluids, from Non-equilibrium Patterns to Cosmic Strings* (Oxford Science, New York, 1999).
- [7] I. S. Aranson and L. Kramer, The world of the complex Ginzburg-Landau equation, *Rev. Mod. Phys.* **74**, 99 (2002).
- [8] E. Sandier and S. Serfaty, *Vortices in the Magnetic Ginzburg-Landau Model* (Springer, Boston, 2008).
- [9] F. Bethuel, H. Brezis, F. Hélein et al., *Ginzburg-Landau Vortices* (Springer, New York, 1994).
- [10] M. C. Cross and P. C. Hohenberg, Pattern formation outside of equilibrium, *Rev. Mod. Phys.* **65**, 851 (1993).
- [11] P. G. de Gennes and J. Prost, *The Physics of Liquid Crystals*, 2nd ed. (Clarendon Press, Oxford, UK, 1993).
- [12] P. Oswald and P. Pieranski, *Nematic and Cholesteric Liquid Crystals* (CRC Press, London, 2005).
- [13] N. Nawa and K. Nakamura, Observation of forming process of bubble domain texture in liquid crystals, *Jpn. J. Appl. Phys.* **17**, 219 (1978).
- [14] S. Pirkel, P. Ribiere, and P. Oswald, Forming process and stability of bubble domains in dielectrically positive cholesteric liquid crystals, *Liq. Cryst.* **13**, 413 (1993).
- [15] P. J. Ackerman and I. I. Smalyukh, Diversity of Knot Solitons in Liquid Crystals Manifested by Linking of Preimages in Torons and Hopfions, *Phys. Rev. X* **7**, 011006 (2017).
- [16] F. Lequeux, P. Oswald, and J. Bechhoefer, Influence of anisotropic elasticity on pattern formation in a cholesteric liquid crystal contained between two plates, *Phys. Rev. A* **40**, 3974 (1989).
- [17] P. Ribiere, S. Pirkel, and P. Oswald, Electric-field-induced phase transitions in frustrated cholesteric liquid crystals of negative dielectric anisotropy, *Phys. Rev. A* **44**, 8198 (1991).
- [18] I. I. Smalyukh, B. I. Senyuk, P. Palfy-Muhoray, O. D. Lavrentovich, H. Huang, E. C. Gartland, Jr., V. H. Bodnar, T. Kosa, and B. Taheri, Electric-field-induced nematic-cholesteric transition and three-dimensional director struc-

- tures in homeotropic cells, *Phys. Rev. E* **72**, 061707 (2005).
- [19] R. Barboza, U. Bortolozzo, M. G. Clerc, S. Residori, and E. Vidal-Henriquez, Optical vortex induction via light-matter interaction in liquid-crystal media, *Adv. Opt. Photonics* **7**, 635 (2015).
- [20] M. G. Clerc, M. Kowalczyk, and V. Zambra, Topological transitions in an oscillatory driven liquid crystal cell, *Sci. Rep.* **10**, 19324 (2020).
- [21] G. Durey, H. R. O. Sohn, P. J. Ackerman, E. Brasselet, I. I. Smalyukh, and T. Lopez-Leon, Topological solitons, cholesteric fingers and singular defect lines in Janus liquid crystal shells, *Soft Matter* **16**, 2669 (2020).
- [22] I. Dierking, *Textures of Liquid Crystals* (Wiley, Hoboken, NJ, 2003).
- [23] M. L. Parra, P. I. Hidalgo, and E. Y. Elgueta, Synthesis and mesomorphic properties of oxadiazole esters derived from (*R*)-2-octanol, (*S*)-2-*n*-octyloxypropanol and (2*S*, 3*S*)-2-chloro-3-methylpentanol, *Liq. Cryst.* **35**, 823 (2008).
- [24] P. Ribiere and P. Oswald, Nucleation and growth of cholesteric fingers under electric field, *J. Phys. (Paris)* **51**, 1703 (1990).
- [25] J. Baudry, S. Pirkel, and P. Oswald, Looped finger transformation in frustrated cholesteric liquid crystals, *Phys. Rev. E* **59**, 5562 (1999).
- [26] S. Thiberge, Structures cholestériques et dynamique hors équilibre, Ph.D. thesis, Université de Nice-Sophia Antipolis, 1999.
- [27] T. Frisch, L. Gil, and J. M. Gilli, Two-dimensional Landau-de Gennes dynamical model for the unwinding transition of a cholesteric liquid crystal, *Phys. Rev. E* **48**, R4199 (1993).
- [28] P. Oswald, J. Baudry, and S. Pirkel, Static and dynamic properties of cholesteric fingers in electric field, *Phys. Rep.* **337**, 67 (2000).
- [29] T. Frisch, S. Rica, P. Couillet, and J. M. Gilli, Spiral Waves in Liquid Crystal, *Phys. Rev. Lett.* **72**, 1471 (1994).
- [30] R. E. Goldstein, G. H. Gunaratne, L. Gil, and P. Couillet, Hydrodynamic and interfacial patterns with broken space-time symmetry, *Phys. Rev. A* **43**, 6700 (1991).
- [31] See Supplemental Material at <http://link.aps.org/supplemental/10.1103/PhysRevResearch.4.L022021> for a video showing the experimental and numerical emergence of labyrinthine patterns from cholesteric fingers.
- [32] J.-S. B. Tai, P. J. Ackerman, and I. I. Smalyukh, Topological transformations of Hopf solitons in chiral ferromagnets and liquid crystals, *Proc. Natl. Acad. Sci. USA* **115**, 921 (2018).
- [33] S. H. Strogatz, *Nonlinear Dynamics and Chaos with Student Solutions Manual: With Applications to Physics, Biology, Chemistry, and Engineering* (CRC Press, New York, 2018).
- [34] F. del Campo, F. Haudin, R. G. Rojas, U. Bortolozzo, M. G. Clerc, and S. Residori, Effects of translational coupling on dissipative localized states, *Phys. Rev. E* **86**, 036201 (2012).
- [35] M. G. Clerc and C. Falcón, Localized patterns and holesolutions one-dimensional extended systems, *Physica A* **356**, 48 (2005).
- [36] R. M. Hornreich, M. Luban, and S. Shtrikman, Critical Behavior at the Onset of k -Space Instability on the λ Line, *Phys. Rev. Lett.* **35**, 1678 (1975).
- [37] J. M. Gilli and L. Gil, Static and dynamic textures obtained under an electric field in the neighbourhood of the winding transition of a strongly confined cholesteric, *Liq. Cryst.* **17**, 1 (1994).